SYNCHROTRON ELECTRON BEAM PARAMETER ANALYSIS

REPORT REVIEW – 2

Final Year Project

by

Naveena Senthil Kumar
(Roll No. 110120077)

Dr. Bhavna Nitin Merh
Scientific Officer/G
Raja Ramanna Centre for Advanced Technology (RRCAT)
Dept. of Atomic Energy
Indore, Madhya Pradesh.

Dr. C.Geetha (Internal Guide)
Assistant Professor
Department of Instrumentation & Control Engineering
National Institute of Technology
Tiruchirappalli.

INSTRUMENTATION AND CONTROL ENGINEERING
NATIONAL INSTITUTE OF TECHNOLOGY
TIRUCHIRAPALLI – 452 013, INDIA

March 2024

Abstract

This work aims to implement and experimentally verify an algorithm for finding the parameters of the synchrotron electron beam and its classification into healthy and unhealthy beam. The parameters are estimated from a sequence of images of the beam's slices. The images are captured perpendicularly to the propagation direction of electron beam on the transport line 1 (TL-1).
In each image, the synchrotron electron beams irradiance is approximated by the two-dimensional Gaussian function. As the next step, a beam's waist location is localized. Classification of beam into categories of healthy and unhealthy this is computed by evaluating the Gaussians' function parameters in ANN model and training it.
The designed algorithms provide satisfactory and reliable results. The precision of the parameter calculated is evaluated by valediction by a generation of a synthetic gaussian image with known parameters and fitting onto the algorithm. Development of wholesome website with a database integration is visioned.

Keywords: Synchrotron electron beam, beam parameters, 2-D gaussian fit, classification.

Contents

Chapter 1
Introduction

This work was created as a part of a B. Tech final year project of laboratory. The project was realized in Raja Rammana Centre For Advanced Technology (RRCAT), Indore in cooperation with the National Institute Of Technology Tiruchirapalli. RRCAT was established by the Department of Atomic Energy, India to expand the activities carried out at Bhabha Atomic Research Centre (BARC), Mumbai, in two frontline areas of science and technology namely Lasers and Accelerators.

Laser: The Centre is also involved in the development of a variety of laser systems and their utilization for applications in industry, medicine and research. The laser systems developed include high power CO2 lasers, flash lamp and diode laser pumped Nd lasers, semiconductor lasers, chemical lasers, excimer lasers and high energy/intensity pulsed lasers.

Accelerator: The Centre has indigenously designed, developed, and commissioned two synchrotron radiation sources: Indus-1 and Indus-2, serving as a national facility. Indus-1 is a 450 MeV, 100 mA electron storage ring emitting radiation from mid-IR to soft x-ray with a critical wavelength of ~61 Å. Indus-2 is a 2.5 GeV electron storage ring designed to produce

x-rays. Synchrotron radiation emitted from its bending magnets has broad spectrum covering soft and hard x-ray regions with a critical wavelength of ~2 Å. With its circumference of 172.5 m, and beam energy of 2.5 GeV, Indus-2 is presently the largest and the highest energy particle accelerator in the country.
The main task of this work was to design an automated algorithm for electron beam parameter estimation. The algorithm should be versatile and should have the scope of working in real time to measure beam parameters, at a reasonably fast rate (1 Hz).

This chapter introduces the BPM, the measuring setup, and the measuring procedure, used in this thesis. Chapter 2 provides an insight into synchrotron systems and gaussian beams. Chapter 3 is dedicated to the proposed algorithms. Experiments and the results are summarized in Chapter 4. In the end, the further targets is in Chapter 6.

1.1 Measuring device setup

The Beam Profile Monitor (BPM) is a diagnostic device designed to observe the transverse profile of an electron beam. It visually displays the beam spot size and shape, aiding operators in steering the beam through transfer lines and initial revolutions in the booster and storage ring. BPMs utilize fluorescence effect, employing a UHV Compatible rotary motion feedthrough to position a 1 mm thick fluorescent ceramic screen (AF995R) in the beam chamber. The beam striking the screen generates fluorescent light, visible through a UHV compatible glass observation window with a video imaging system. Multiple BPMs are installed in the Indus-1 accelerator system, including Transfer Line-1 (TL-1), Booster Synchrotron, and Transfer Line-2 (TL-2). Operators can select and monitor beam spots via video monitors in the control room, with the option to capture data for later analysis using in-house software. Recent upgrades include four improved BPMs in TL-1 and TL-2, enhancing performance and features.

Figure 1.1:(a)Fluorescent ceramic (AF995R) assembled Figure 1(b)TL-1 Beam Profile Monitor

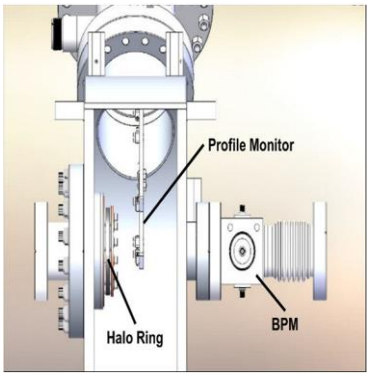

Figure 1.2. Schematic of beam position monitor

Chapter 2
SYNCHROTRON

In this work, the designed algorithm should approximate electron beam Gaussian parameters. Therefore, it is convenient to discuss what a synchrotron is and its essential structure and beamline properties.

A synchrotron is a particular type of cyclic particle accelerator, descended from the cyclotron, in which the accelerating particle beam travels around a fixed closed-loop path. The magnetic field which bends the particle beam into its closed path increases with time during the accelerating process, being synchronized to the increasing kinetic energy of the particles. The synchrotron is one of the first accelerator concepts to enable the construction of large-scale facilities, since bending, beam focusing, and acceleration can be separated into different components. The synchrotron evolved from the cyclotron, the first cyclic particle accelerator. While a classical cyclotron uses both a constant guiding magnetic field and a constant-frequency electromagnetic field (and is working in classical approximation), its successor, the isochronous cyclotron, works by local variations of the guiding magnetic field, adapting to the increasing relativistic mass of particles during acceleration.

In a synchrotron, this adaptation is done by variation of the magnetic field strength in time, rather than in space. For particles that are not close to the speed of light, the frequency of the applied electromagnetic field may also change to follow their non-constant circulation time. By increasing these parameters accordingly as the particles gain energy, their circulation path can be held constant as they are accelerated. This allows the vacuum chamber for the particles to be a large thin torus, rather than a disk as in previous, compact accelerator designs. Also, the thin profile of the vacuum chamber allowed for a more efficient use of magnetic fields than in a cyclotron, enabling the cost-effective construction of larger synchrotrons.

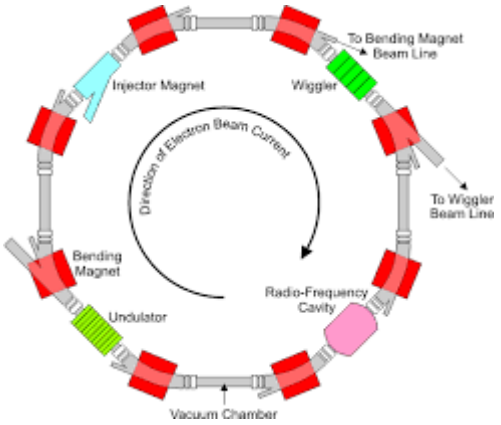

Figure 2.1 Schematic of a synchrotron.

2.1 Structure Of Synchrotron

A synchrotron is a powerful machine that accelerates charged particles to nearly the speed of light. It has a complex structure consisting of several key components like Storage Ring, Magnets ,Radiofrequency Cavities , Beamline etc.

A Storage Ring is a donut-shaped ring where the particles travel at high speeds. The ring is made of sections of straight tubes connected by bending magnets. Synchrotrons use a series of magnets to bend and focus the beam of particles. Radiofrequency (RF) Cavities accelerate the particles as they travel around the ring. After This, The path taken by X-rays take after they are produced by the synchrotron is known as Beamline.

In addition to these main components, synchrotrons may also include other components which make them more effective.

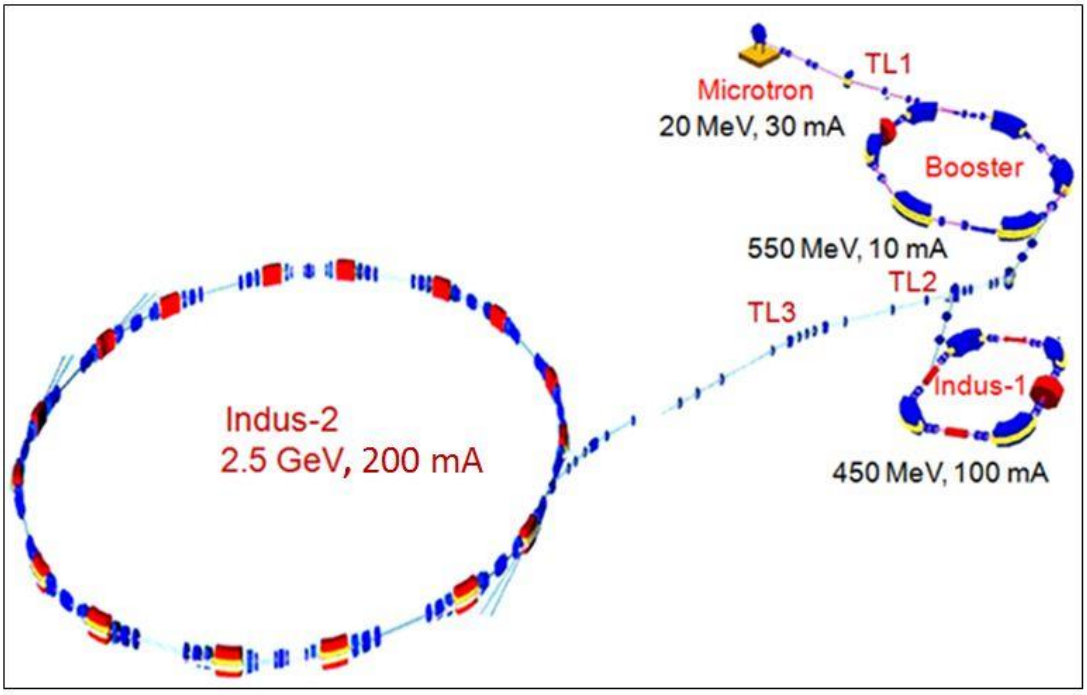

Figure 2.2. A schematic of the Indus Accelerator Complex

2.1.1 Indus 1

Fig.2.3 shows a view of Indus-1 storage ring. It has a circumference of 18.97 m in which four combined function 90° bending magnets and 16 quadrupole magnets are arranged in four identical cells. Each unit cell has a 1.3 m long straight section. Two straight sections are used for beam injection; one section accommodates the septum magnet and the other, diametrically opposite to it, has a pulsed kicker magnet to inject electron beam into the ring. Another straight section accommodates an RF cavity operating at a frequency of 31.613 MHz. Synchrotron radiation is tapped from 3

bending magnets. Each bending magnet vacuum chamber has 2 ports, one at 10° and another at 50° for tapping the emitted synchrotron radiation.

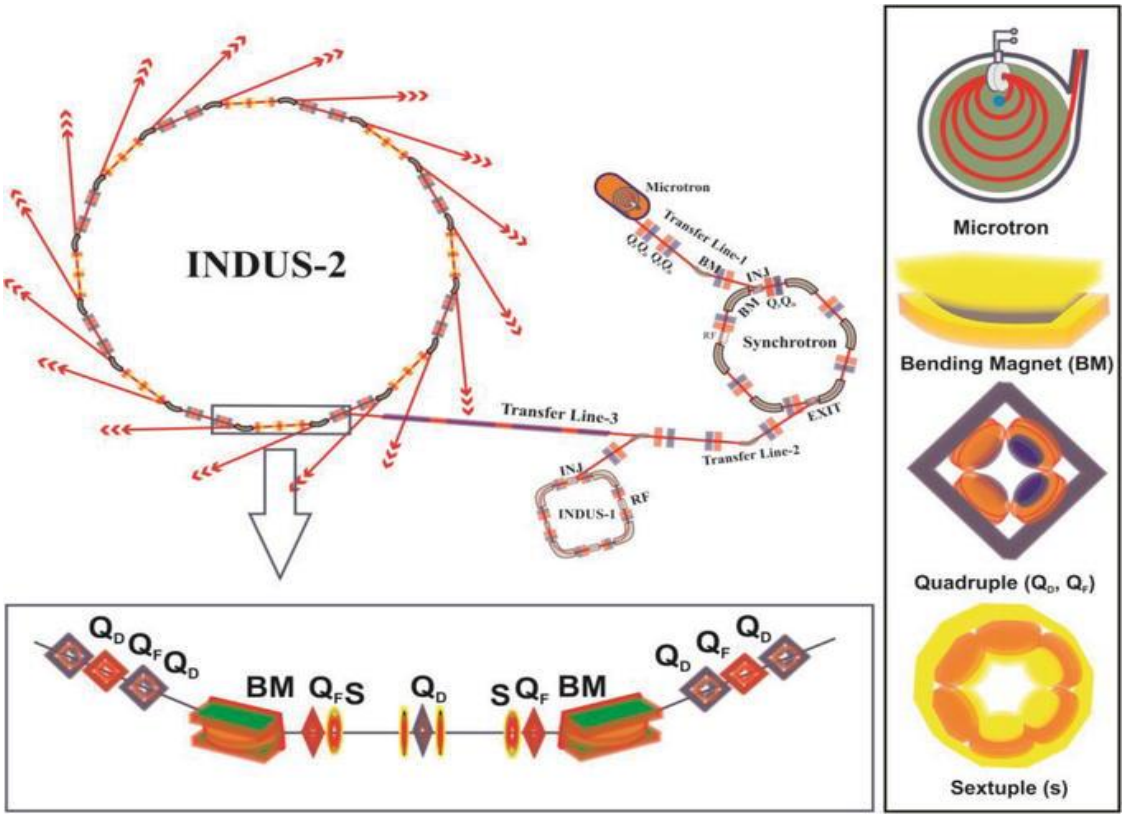

Figure 2.3 : a) Indus 1 at RRCAT b) Indus 2 schematic c) Indus 2 Ring

2.1.1 Indus 2

INDUS-2 is a high-brightness X-ray source operating at a beam energy of 2 GeV. It features an expanded Chasman Green lattice, optimized to accommodate multiple insertion devices. The storage ring comprises 8-unit cells, each offering a 4.5 m long straight section. The magnetic structure of INDUS-2 includes two 22.5° bending magnets per unit cell, along with quadrupole and sextupole elements for beam control and correction. Notably, the lattice design includes ample space between focusing and defocusing quadrupoles for accommodating beam diagnostic and vacuum devices. For detailed design parameters, refer to table 2.

Table 2. Parameters of INDUS-2.

Energy	: 2 GeV
Current	: 300 mA
Bending field	: 1.2 T
Critical wavelength (l_c)	: 3.88 Å (BM)
	: 0.93 Å (Wavelength shifter)
	: 2.59 Å (MW)
Circumference	: 172.2781 M
Typical tune point	: 9.2, 5.2
Beam emittance ε_x	: 3.72×10^{-8} m.rad
ε_y	: 3.72×10^{-9} m.rad
Electron beam size and divergence	
Centre of bending magnet σ_x, σ_y	: 0.187, 0.190 mm
$\sigma_{x'}$, $\sigma_{y'}$	: 0.287, 0.050 mrad
Centre of insertion section σ_x, σ_y	: 0.722, 0.086 mm
$\sigma_{x'}$, $\sigma_{y'}$	: 0.052, 0.043 mrad
Bunch length $2\sigma_l$	: 3.00 cm
Beam lifetime	: 20.0 hours
Energy spread	: 7.2×10^{-4}
Revolution frequency	: 1.740 MHz
RF frequency	: 189.678 MHz
Harmonic number	: 109
Power loss	: 76.3 kW (BM)
	: 4.3 kW (WSH)
	: 5.2 kW (MW)

BM: Bending magnet; MW: Multipole Wiggler (1.8 T); WSH: Wavelength shifter (5 T).

2.2 Beam & Beamline

Beamline refers to the path that the X-rays or other particles take after they are produced by the machine.

It's essentially a long tube that a) Guides the beam of particles or X-rays b) Houses various equipment used to manipulate and focus the beam c) Leads to the experimental stations, where the beam is used for research purposes. The common elements found in beamlines include:

- Collimators: These devices help to shape and focus the beam of particles or X-rays.
- Monochromators: These devices select a specific range of wavelengths from the beam.
- Mirrors and lenses: These elements are used to focus and direct the beam towards the experiment.
- Detectors: These instruments measure the properties of the beam after it interacts with the sample being studied.

2.2.1 Properties of Beam

Synchrotron light has a number of unique properties. These include: High brightness: synchrotron light is extremely intense (hundreds of thousands of times more intense than that from conventional x-ray tubes) and highly collimated. Wide energy spectrum: synchrotron light is emitted with energies ranging from infrared light to hard x-rays. Tunable: it is possible to obtain an intense beam of any selected wavelength. Highly polarized: the synchrotron emits highly polarized radiation, which can be linear, circular or elliptical. Emitted in very short pulses: pulses emitted are typically less than a nano-second (a billionth of a second), enabling time-resolved studies.

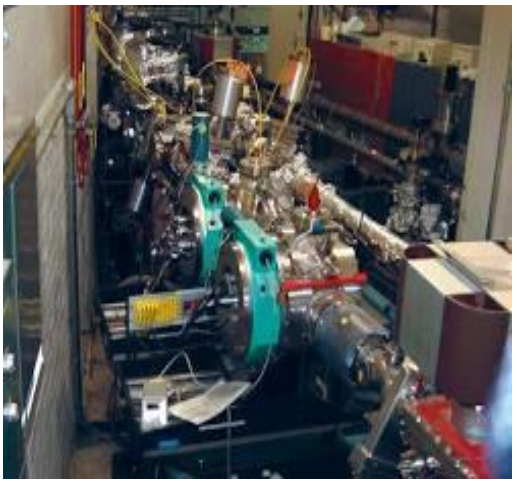

Figure 2.4 : Beamline Indus 1 at RRCAT

2.2.2 Applications of Beamline radiation

CAT/BARC is constructing five beamlines with diverse applications. The Metrology beamline utilizes a toroidal grating monochromator to cover a wavelength range from 40 Å to 1000 Å, serving as a general-purpose beamline with a reflectometer end station for checking reflectivity of optical elements. The Photo physics beamline, based on a Seya Nomioka monochromator, spans from 150 Å to 3000 Å, enabling time-resolved spectroscopy. Additionally, the VUV spectroscopy beamline employs a 6.65-meter off-axis Eagle mount spectrograph, covering a photon energy range from 9 eV to 990 eV, offering high-resolution spectroscopic analysis.

2.3 Stigmatic Gaussian beam

A Gaussian beam is the fundamental solution to the paraxial wave equation, as derived in [6] p. 54-57 from Maxwell's equations. The beam's angular divergence is the smallest, and a lens can focus it down to the smallest-sized spot. For convenience, the beam's propagation axis is often regarded as the z axis.

A stigmatic model of the Gaussian beam is the simplest. It assumes that the beam has a circular irradiance pattern (rotationaly symetric) in the cross-section perpendicular to the propagation axis. Moreover, it is said to have a spherical or a flat wavefront at every point of its propagation distance. For a monochromatic beam, propagating in the z direction with the wavelength λ,the complex electric field amplitude (phasor) as described in [8] is:

$$E(r,z) = \frac{E_0\,\omega_0}{\omega(z)} \cdot \exp\left(-\frac{r^2}{\omega^2(z)} + i\left[kz - \arctan\left(\frac{z}{z_R}\right) + \frac{kr^2}{2R(z)}\right]\right) \tag{1}$$

where $|E_0|$ is the peak amplitude and ω_0 is the beam radius at the beam waist, and $k = \frac{2\pi}{\lambda}$ is the *wavenumber*. The parameter r is the radial coordinate of a wavefront point in the plane perpendicular to the propagation axis. The x_R is Rayleight length, and the radius of curvature $R(x)$ of the wavefronts, described below. In each z-plane, the transverse beam profile is again a Gaussian of width $\omega(z)$.

Diameter

A beam emitted has some *diameter* .There are different metrics, that address problem of defining it. The most used is the $1/e^2$ *width*, it corresponds to twice the waist size $\omega(z)$ (as in equation (1)). It can be computed as

$$\omega(z) = \omega_0\sqrt{1 + \left(\frac{z}{z_R}\right)^2}, \tag{2}$$

where the *waist spot size* ω_0 is the smallest value of the beam's radius at the beam waist position ($x = 0$ for stigmatic Gaussian beams) [3]. The x_R is the *Reighley range* [3]

$$z_R = \frac{\pi\omega_0^2}{\lambda}. \tag{3}$$

Sometimes other measurements are used, such as a so-called *Full Width at Half Maximum* (FWHM, the diameter at half the maximal intensity) or $1/e$ *width*, shown in Fig. 2.5.

Divergence

The diameter varies across the beam as it propagates. The divergence of a Gaussian beam can be calculated as in [3]

Practically, the divergence of a beam can be measured. The first approach measuresthe beam spreading angle at considerable distances from the source (in the far field of the laser beam). The second approach is applicable in cases when an aberration-freelens focuses a laser beam down. It measures the beam width ω_f in the focal plane of the lens. The according to [9] the divergence angle is determined by equation $\vartheta = w_f/f$, where f is the focal length of the lens.

A *collimated beam* of light is a beam propagating in a homogeneous medium with a low beam divergence so that the beam radius does not undergo significant changes within moderate propagation distances. In the case of Gaussian beams, the article [8] states that the Rayleigh length must be long in comparison to the propagation distance. It is impossible to generate an ideal collimated beam by additional optics since the Gaussian beam always has a finite divergence angle and diverges under free-space propagation.

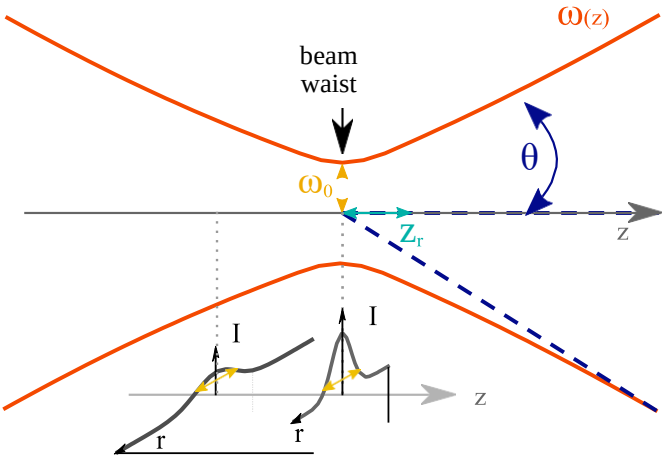

Figure 2.5. Gaussian's beam waist along propagation axis (z-axis).

Radius of curvature

The phase of the laser beam's field distribution is always spherical due to the paraxial approximation. As stated in [5] vol. 2 its dependence on the propagation distance x is given by *radius of curvature* of the wavefront:

$$R(z) = z + \frac{z_R^2}{z}. \tag{4}$$

At the beam waist position, the phase is constant, therefore the radius of curvature is infinite. While far away from the waist, the phase function is concentric to the waist position. The minimum radius of curvature is attained at the Rayleigh distance with $R_{min} = 2x_R$.

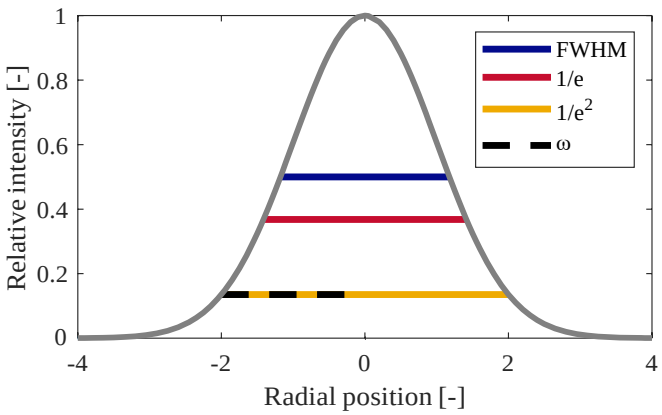

Figure 2.6. Paraxial Gaussian's beam Full Width Half Maximum, $1/e^2$ width and waist.

2.4 Orthogonal astigmatic Gaussian beams

As stated in [7], orthogonal astigmatic Gaussian beams have elliptical irradiancespots and ellipsoidal wavefronts at every point along the propagation. Unlike in thecase of a stigmatic Gaussian beam, circular cross-sections are only achieved in few specific points. The orientation of irradiance, represented by a beam spot, coincides with the orientation of wavefronts. Both orientations remain unchanged as the beam propagates through a homogeneous medium. Therefore, such beams have two planes of symmetry, corresponding to the principal semi-axes of the irradiance pattern or the wavefront. In general case, the parameters may differ for each axis.

A complex parameter q that is introduced below is often used in combination with the so-called *ABCD* matrix to describe the propagation of such Gaussian beams.

2.5 Beam Imaging System

A beam imaging system is a technology used to visualize and characterize beams of particles or radiation.In Indus accelerators, a number of beam diagnostic devices have been installed which are used during regular machine operation, machine experiments and studies. Beam profile monitors (BPMs) are used for visual observation of transverse shape, orientation and position of the beam in transfer lines and the storage rings. They use a fluorescent screen made of chromium-doped alumina, which can be inserted into the beam path and the spot generated by fluorescent light generated is viewed by a CCD The beam position data obtained from these BPIs is used to define and correct the beam orbit.

Chapter 3
Algorithm for beam's parameters estimation

This work aimed to propose, implement, and experimentally verify an algorithm for finding the electron beam's parameters from a sequence of images. The sequence represents the eelctron beam's slices in the the x axis, as described {{in section 1.2.}}

Some of these parameters may be measured by using a camera setup.The international standard [9] describes test methods and principles for measuring beam width, divergence angle of a laser beam which is taken into consideration and incorporated here. It states that,

1) The optical axis of the measuring system should be coaxial with the measured laser beam.
2) The attenuators or beam-forming optics should be mounted such that the opticalaxis runs through the geometrical centers.
3) The aperture of the optical system should accommodate the entire cross-section of the laser beam.

Moreover, for pixel-based detector systems, the spatial resolution should be at least 1/20 of the beam width.

The setup for our experiments has been primarily used for determining the center point position and estimating gaussian parameters of the emitted electron beam. This estimation will require two steps, firstly a parametric description of a single image should be acquired. In the second step, extracted parameters from the fitted functions are processed to estimate the parameters.

3.1 State of the art

A standard industry method of measuring the beam's profile has been the use of a pinhole technique. The pinhole is used to samplethe beam's intensity by mechanically moving an aperture across the beam in a plane orthogonal to the optical axis. In 2013 a modified technique was proposed in article [01]. The improvement in CCD cameras, the new profilers based on two-dimensional photo-detectors were introduced. Article [20] authors designed and tested a simple automated setup for measuring the profile and spot size of a Gaussian laser beam. Two standard profiling techniques were implemented, the imaging technique for the CMOS 2D array and the scanning knife-edge-like technique for the single photodiode. Authors claim that the results of the knife-edge-like technique have proved to produce more stable results. However, the CCD camera's beam's waist error, around 1%, is still reasonably small. A comprehensive summary of the available methods is described in [21].

In [23], the author dealt with imaging a laser beam by a CCD camera.

Figure 3.1. ECS Digital Microscope CCD Camera

3.2 Proposed algorithms

The intensity in the acquired images represents an irradiance cross-section of the Gaussian beam perpendicular to the propagation axis (x-*cut*). The intensity will be approximated by bivariate Gaussian function. Gaussian standard deviations σ_x, σ_y (which correspond to $\omega_x(x)/2$, $\omega_y(x)/2$ for orthogonal astigmatic Gaussian beams and Gaussian center position x_o, y_o will be extracted from the x-cut to determine the parameters.

A Gaussian function was fitted to each image in the sequence of the beam slices.If the Gaussian's curve fit was sufficiently good, the results were processed as follows:

1)Extract sequence of Gaussian's standard deviations σ, which are acquired by bivariate Gaussian distribution fitting (section 3.3)
2)Find the global minimum of the chosen σ sequence.
3)Find the sequence of Gaussian's center coordinates $[x_o, y_o]$.

3.3 Bivariate Gaussian distribution fitting

A bivariate Gaussian function estimates the beam irradiance profile .We can describe the Gaussian function in the following parametrization:

$$G(x, y) = A \exp\left(-\frac{1}{2}\left(\frac{(x - x_o)^2}{\sigma_x^2} + \frac{(y - y_o)^2}{\sigma_y^2}\right)\right) . \tag{3.1}$$

The coefficient A is the amplitude, x_o, y_o are the coordinates of the center and σ^2_x and σ_y^2 are the variances in x and y directions. This equation is capable of producing.

only such elliptical Gaussian function. In more general case, the coordinates can be rotated by angle ϑ around x axis. Such rotation can be represented by a rotation matrix This rotation can be represented by a rotation matrix. The rotation matrix transforms the original coordinates (x, y) to the rotated coordinates as follows:

$$\begin{matrix} x_{rot} \\ y_{rot} \end{matrix} = \begin{matrix} \cos\vartheta & -\sin\vartheta \\ \sin\vartheta & \cos\vartheta \end{matrix} \begin{matrix} \hat{x} \\ \hat{y} \end{matrix} = \begin{matrix} \cos(\vartheta)\,\hat{x} + \sin(\vartheta)\,\hat{y} \\ \sin(\vartheta)\,\hat{x} + \cos(\vartheta)\,\hat{y} \end{matrix} . \tag{3.2}$$

Where $\hat{x}$ denotes $x - x_o$ likewise the $\hat{y} = y - y_o$. Therefore, if one substitutes the rotated coordinates into equation (3.1) the expression takes form.

Offset

Due to the technical properties of the cameras, the base level of pixel read-out is not equal to zero. Therefore, an offset parameter I_o was introduced into the Gaussian function (3.3) for actual fitting:

$$G^*(x, y) = G(x, y) + I_o. \tag{3.4}$$

One possibility of dealing with the offset is to estimate and subtract that parameter before computing the Gaussian's parameters. However, determining the exact value of that parameter can prove to be quite tricky. Even for imaging a uniform homogeneous background, the pixels' irradiance values differ from each other. In theory, this irregularities should adhere to the Poisson distribution. Which makes it insufficient to

sample this parameter only from one value. The exact implementation of this parameter estimation is described in section 3.3.1.

3.3.1 Statistical solution

One possible way of estimating a Gaussian function is to consider each statistical properties of each image. A region of an image is created, that contains only the reasonable neighborhood of Gaussian beam's center. We have decided, to determine the corresponding region by thresholding the pixels intensity levels. After several experiments with our datasets, in which we examined the changes of the computed standard devia- tions between images in the captured sequence, we have decied to only the pixels, whose values are in the upper 90 % of the maximal intensity will be fitted. Their convex hull will define the fitting region.

Parameters' limits

The non-linear least squares (non-linear *LSQ*) algorithm was used for fitting the Gaussian curve with added offset value $G^*(x, y) = G(x, y) + I_o$, where $G(x, y)$ is defined as in equation (3.10). An algorithm was implemented in the scripting language Python 3.7 using the library scipy. A method used in implementing the non-linear least squares constrained solution is based on Trust Region Reflective method, that is motivated by the process of solving a system of equations, which constitute the first-order optimality condition for a bound-constrained minimization problem. More specifications of the used LSQ algorithm can be found in [28].

The Trust Region Reflective method needs to be provided with the parameter's limits. They were set to:

- x_o, y_o .....⟨0, image's height⟩, ⟨0, image's width⟩.
- σ_x, σ_y..... ⟨1, image's height/2⟩, ⟨1, image's width/2⟩.
- ϑ ..... ⟨0, π/2⟩.
- A.....⟨minimal pixel value, number of camera's available gray levels⟩.
- I_o.....⟨minimal pixel value−5, maximal pixel value⟩.

Initial guess

The results were proven to be highly affected by the initial guess of the Gaussian parameters. In the simplest case, the initial guess was set based on the observations of the datasets. This method will be referenced to as the *Max*:

- x_o, y_o .....brightest pixel position.
- σ_x, σ_y ..... 10, 10.
- ϑ.....0.
- A ..... difference between the brightest and the darkest pixel.
- I_o.....image's lowest intensity value

This provided a better initial guess of the parameters. The ellipse fitting was implemented using the OpenCV Python module. Firstly, the image was thresholded by value 245 in a 8 bit grayscale value ranging from [0,255] highest recorded intensity in the image.

Then the connected components in the 8-neighbourhood are found. Lastly, the contour of the largest component is found to which an ellipse is fitted in the least-squares sense. The initial guess estimation method Ellipse then sets Gaussian's parameters to:

- x_o, y_o .....ellipse's center point position.
- σ_x, σ_y..... half-lengths of the ellipses diagonals.
- ϑ ..... ellipse's rotation angle.
- A ..... difference between the brightest and the darkest pixel.
- I_o .....image's lowest pixel value.

Chapter 4
Software Results

This chapter evaluates the overall performance of the designed algorithms. On top of that, it assesses algorithms' speed and robustness to image noise. Various experiments were conducted as the means of assessing the behavior of proposed algorithms under different circumstances. A synthetic image was generated and tested.

4.1 Compared algorithms

Within the scope of this work, three algorithms for estimating the Gaussian beam's parameters were proposed. Two of which are of an iterative kind, based on non-linear least squares (LSQ) fitting. The last one is based on the estimation of covariance matrix directly from the dataset, according to equation (3.6). The iterative algorithms need to be provided with an initial parameter estimate (*initialguess*), from which the parameter optimization is carried on. The method of determining these parameters were introduced in section Initial guess. It is based on the extreme irradiance pixels in the image (regarded as *Max*).

4.2 Datasets

For the testing purposes of the Gaussian function fitting, three synthetic datasets (D1, D2, D3) were created artificially. The images of the Gaussian 2D function were generated in python with a size of (400×250) px, re-casted as uint8 type, and saved in TIFF format,see Fig. 4.1.

- D1 dataset contains three generated images with known Gaussian parameters. The first two images were designed to determine the algorithm's ability to correctly estimate an ideal Gaussian function with varied sigma and position, shown in Fig. 4.1.

- D2 dataset was designed to measure accuracy of processing a sequence of images, with introduced Gaussian noise see Fig. 4.2. A set of twenty-five images was generated.

- D3 dataset was designed to measure accuracy of processing a sequence of images, with introduced Salt and pepper noise see Fig. 4.3. A set of twenty-five images was generated.

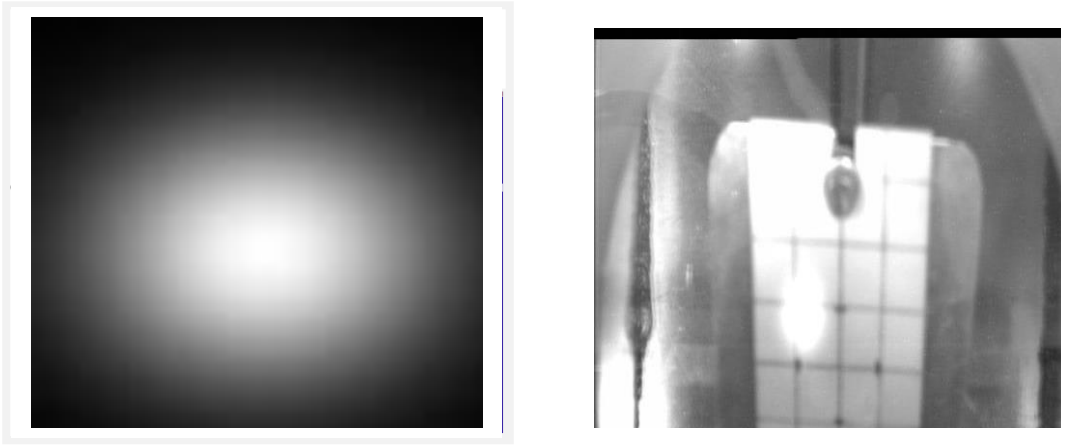

a) Synthetic Image b) Image added onto dark frame

Figure 4.1. a) Synthetic Image generated with known parameters; b) synthetic beam image added on to the screen image.

Addition Of Noise

Salt and pepper noise is added to the image with parameters ranging from 0.08 to 0.1 .This noise manifests as randomly scattered white and black pixels, with the number of salt and pepper pixels determined by the calculation. In contrast, Gaussian noise with a standard deviation of 10 is added to each pixel of the image, resulting in continuous random variations around the original pixel values. Salt and pepper noise introduces extreme outliers, while Gaussian noise adds a smoother distribution of variations.

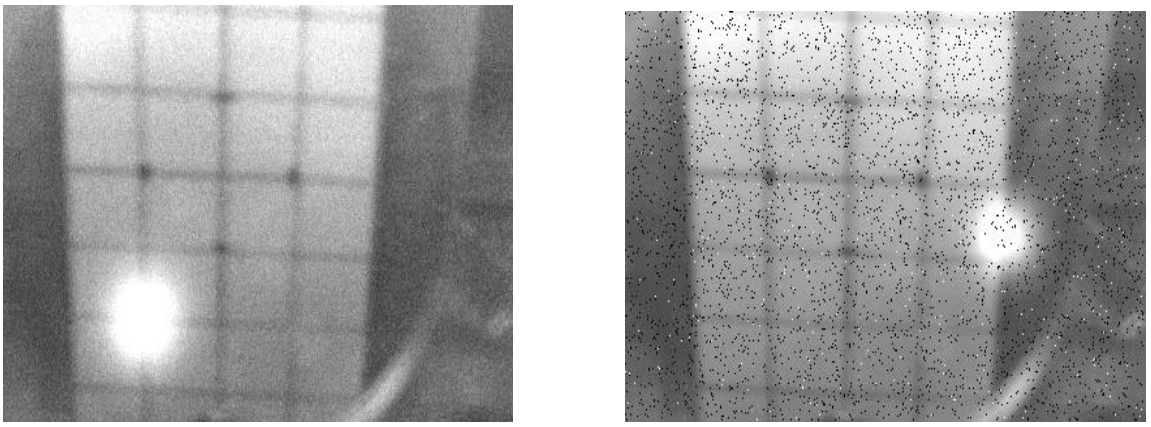

a) Dataset D2 with Gaussian noise. **b)** Dataset D3 with Salt & Pepper noise

Figure 4.2. Addition of noise onto synthetic images to make the images more ideal.

Exporting data

For the datasets D1, D2, and D3, the parameters for Gaussian noise varied, as evidenced by the output in the Python code terminal. To facilitate further processing, these parameter values were exported to an Excel file with the (.xlsx) extension and saved. Furthermore, the images along with their respective parameters are awaiting training in an Artificial Neural Network (ANN) model configuration designed for the classification of healthy and unhealthy beams. the iterative algorithms to fail. Even though the algorithms with the initial guesses

	A [-]	x_0 [px]	y_0 [px]	σ_x [px]	σ_y [px]
			Synthetic Image: without noise		
Image 1	12 257.27	138.00	105.00	40.64	10.11
Image 2	9 827.26	138.00	105.00	21.08	19.25
Image 3	12 257.26	138.00	105.00	40.64	10.11
Image 4	12 257.26	138.00	105.00	40.64	10.11
Image 5	12 257.26	138.00	105.00	40.64	10.11
Image 6	12 252.67	138.00	105.00	35.80	9.97
			Synthetic Image: with noise		
Image 1	12 257.27	138.00	105.00	40.64	10.11
Image 2	11 400.29	138.00	105.00	34.52	11.87
Image 3	12 257.26	138.00	105.00	40.64	10.11
Image 4	12 257.29	138.00	105.00	40.64	10.11
Image 5	12 257.29	138.00	105.00	40.64	10.11

Table 4.1. Gaussian's parameters on three generated test-images from D1,D2,D3 dataset.

4.2 Preprocessing

A set of generated synthetic images with preprocessed in various imaging preprocessing steps. Initially, the grayscale image is loaded and cropped to a target resolution of 250x400 pixels. Gaussian noise is fitted to the cropped image to model its intensity distribution. Contrast enhancement is applied using Contrast Limited Adaptive Histogram Equalization (CLAHE). Subsequently, thresholding is performed to segment the beam, followed by contour detection to identify the largest contour, assumed to be the beam. The beam region is extracted using a mask and intensity profiles along the x and y axes are computed.

To ensure valid results and accurate preprocessing, preprocessing steps were done using OpenCV as well as Image J software. Fig 4.3 shows the all 4 steps accomplished in both the softwares.

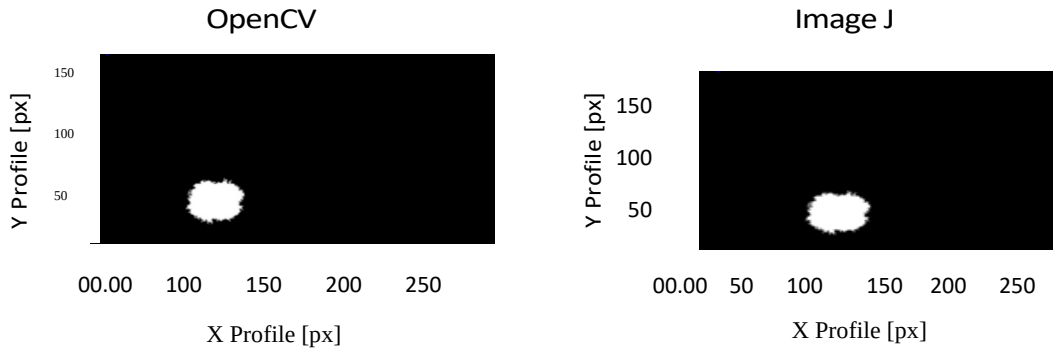

Figure 4.3. Computed inclination angle for generated dataset D2.

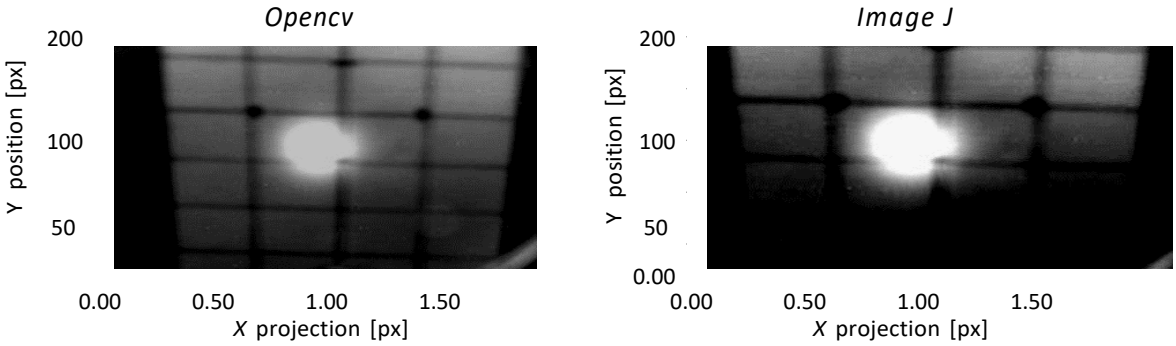

a) OpenCV - CALHE b) IMAGE J - CALHE

Figure 4.4. Effects of Contrast Limited Adaptive Histogram Equalization (CLAHE).

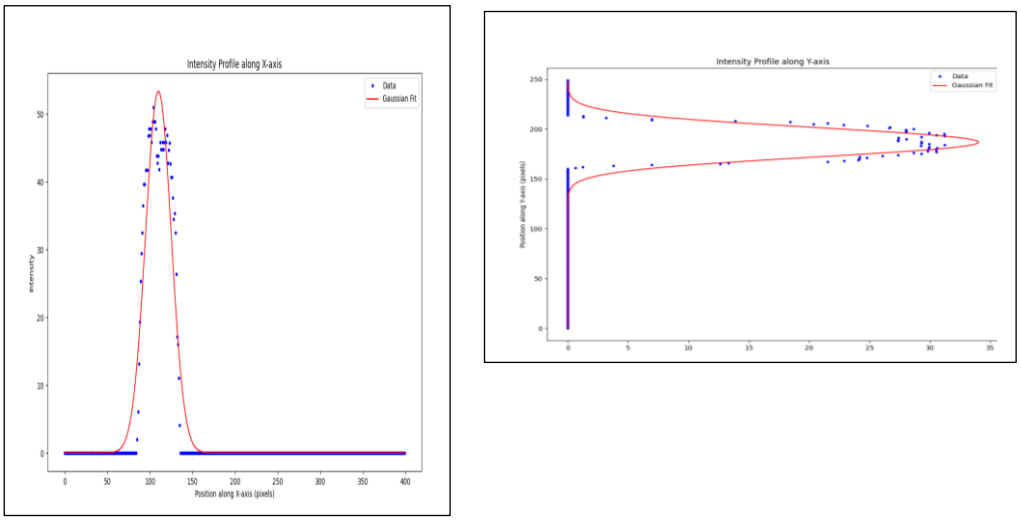

Figure 4.5. Intensity profile X & Y axis resp.

4.3 Goodness of Gaussian fit

Three algorithms for estimating the Gaussian beam parameters were tested on the generated dataset D1 that was described above, compared reference values (ground truth) to the values that were fitted by the algorithms.

The Direct algorithm in combination with Max initial guess estimate produced partially incorrect results in the first image. The initial guess of the standard deviations (σ_x, σ_y) and the ϑ angle were significantly off in comparison to the ground truth.

Originie software serves as a pivotal tool within the realm of scientific inquiry, facilitating rigorous data analysis and visualization. Embedded within its suite of functionalities is the capability to execute Gaussian fits on datasets and extract parameters. Fig 4. Shows the fit of gaussian onto the dataset.

As for the results of the Statistical algorithm in the first image, the offset of the estimated Gaussian's standard deviation parameters is likely to be caused by the factthat the the Gaussian is located close to the image's edge. Part of the values relevantfor fitting were cropped by the image frame. This should not pose a problem for the algorithm for most micro-modules, as they are imaged so that their projection in the region near the focal point is close to the image's center. The images taken further from the focal point are discarded by an IOA criterion in any case.

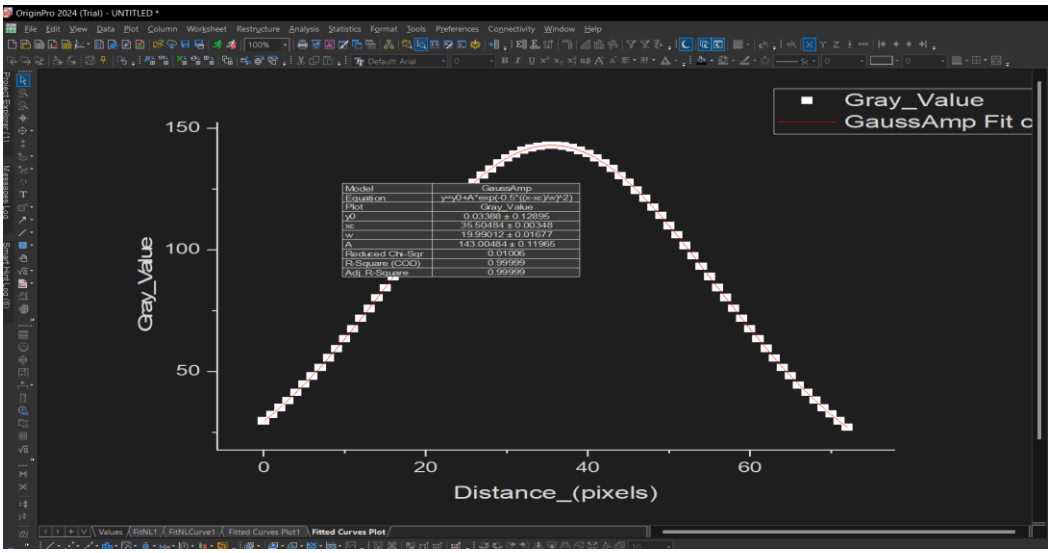

Figure 5.3. Fitted Gaussian curves to D1 dataset on origine software. Red lines represent fit on the data; along with the parameter details

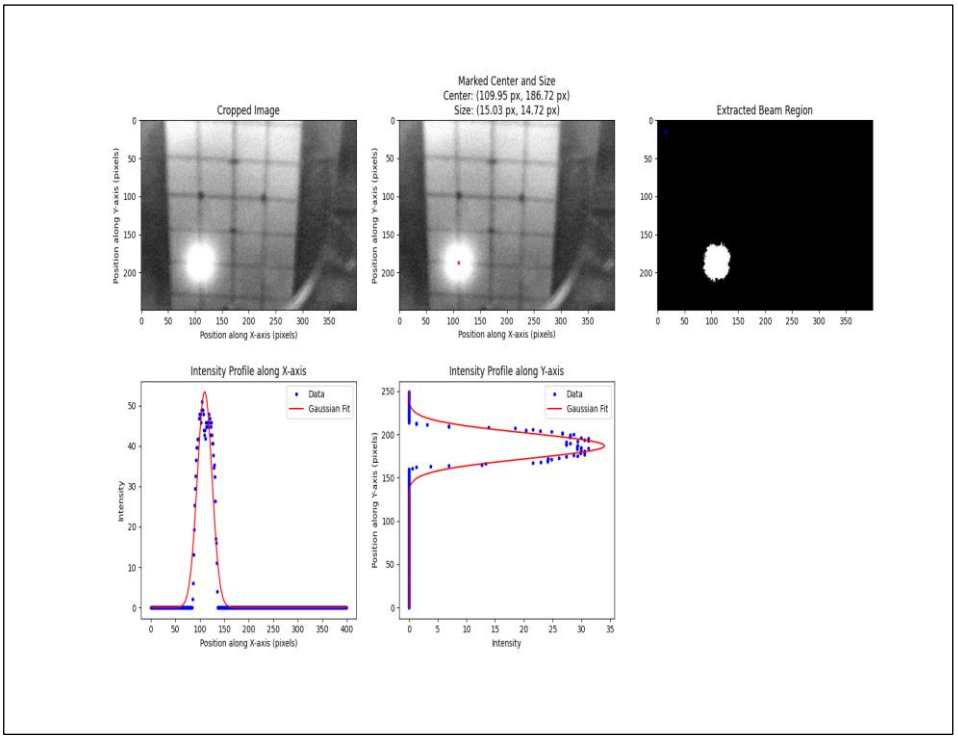

Figure 5.4. Fitted Gaussian curves to D1 dataset using Scipy lib. Subplot a) cropped image (specific for processing) b) estimated center and size of beam d) & e) Intensity fit on the data on the axis X & Y resp.;

Chapter 5
Further Work

This Review 2 work focuses on estimating the parameters of a beam emitted by a micro-module. The algorithm, designed to determine the electron beam'sposition and classify into healthy/unhealthy beam, evaluates the parameters extracted from the entire sequence of images. The algorithms that approximate beam cross-sectionby a two-dimensional Gaussian function operate at the level of a single image.

An algorithm was proposed for the Gaussian function fitting. It was tried on the synthetic generated image, the gaussian parameters extracted were compared with the true values , the algorithm was robust and within minimal error .Further steps involves achieves second goal of the aim , training a ANN model with the parameters obtained from the gaussian fit and testing out with the real data set is the upcoming target. Along with a classification model which classifies the beam into healthy and unhealthy depending upon the parameters is yet to be achieved.

Developing a fully indigenous website entails leveraging PostgreSQL as the database management system. This robust platform ensures efficient data storage and retrieval, critical for web applications. Integrating Spring Boot and Java further enhances functionality, providing a seamless framework for building and deploying the website. Additionally, the incorporation of image extraction with a date filter adds a sophisticated layer of data processing. By extracting parameters from images based on specified dates, users can access and analyze relevant information in a dynamic and user-friendly interface. These are the targets set to be fulfilled in the upcoming days.

References

[1] HECHT, J. *Understanding lasers*. 4. ed. Piscataway, NJ: IEEE Press, 2019. ISBN 978-1-119-31064-8.

[2] HECHT, E. *Optics*. England, UK: Pearson Education, Incorporated, 2017. ISBN 978-1-292-09693-3.

[3] SVETLO, O. *Principles of Lasers*. 5. ed. New York: Springer, 2010. ISBN 978-1-4419-1301-2.

[4]

[5] GROSS, H. *Handbook of Optical Systems.* 1. ed. Weinheim: Wiley-vch, 2005. ISBN 35-274-0378-5.

[6] CHANG, W. S. C. *Principles of lasers and optics*. Cambridge: Cambridge University Press, 2007. ISBN 05-216-4535-2.

[7] KOCHKINA, E. *Stigmatic and Astigmatic Gaussian Beams in Fundamental Mode*.

[8] PASCHOTTA, R. *Gaussian Beams*. [cit. 2022-03-28]. https://www.rp-photonics.com/gaussian_beams.html.

[9] *Lasers and laser-related equipment - Test methods for laser beam widths, divergence angles and beam propagation ratios*.

[10] PASCHOTTA, R. *Gouy Phase Shift*. [cit. 2022-03-28]. https://www.rp-photonics.com/gouy_phase_shift.html.

[11] *Laser Optics Resource Guide*. [cit. 2022-03-25]. https://www.edmundoptics.com/knowledge-center/application-notes/lasers/laser-optics-resource-guide/.

[12] CAI, Y., and Q. LIN. The elliptical Hermite-Gaussian beam and its propagation through paraxial systems. *Optics Communications*. 2002, Vol. 207, No. 1, pp. 139-147. Available from DOI https://doi.org/10.1016/S0030-4018(02)01533-X.

[13] MEI, Zh., J. GU, and D. ZHAO. The elliptical Laguerre-Gaussian beam and its propagation. *Optik*. 2007, Vol. 118, No. 1, pp. 9-12. Available from DOI 10.1016/j.ijleo.2005.12.012.

[14] NASSE, M. J., and J. C. WOEHL. Realistic modeling of the illuminationpoint spread function in confocal scanning optical microscopy. *J. Opt. Soc. Am. A*. OSA, Feb, 2010, Vol. 27, No. 2, pp. 295–302. Available from DOI 10.1364/JOSAA.27.000295.

[15] SAKURAMBO. *Airy-pattern.svg*. https://commons.wikimedia.org/wiki/File:Airy-pattern.svg.

[16] PASCHOTTA, R. *Optical Aberrations*. [cit. 2022-03-28]. https://www.rp-photonics.com/optical_aberrations.html.

[17] SCHMIDT, J. D. *Numerical simulation of optical wave propagation with examples in MATLAB*. 1. ed. USA: SPIE, 2010. ISBN 978-0-8194-8326-3.

[18] SHEU, F.-W., and Ch.-H. CHANG. Measurement of the intensity profile of a Gaussian laser beam near its focus using an optical fiber. *American Journal of Physics*. 2007, Vol. 75, No. 10, pp. 956-959. Available from DOI 10.1119/1.2723797.

[19] HOSSAIN, Md A., J. CANNING, K. COOK, and A. JAMALIPOUR. Smartphone laser beam spatial profiler. *Opt. Lett.* OSA, Nov, 2015, Vol. 40, No. 22, pp. 5156–5159. Available from DOI 10.1364/OL.40.005156.

[20] BONNETT DEL ALAMO, M., C. SONCCO, R. HELACONDE, J. L. BAZO ALBA, and A. M. GAGO. Laser spot measurement using simple devices. *AIP Advances*. 2021, Vol. 11, No. 7, pp. 075016. Available from DOI 10.1063/5.0046287.

[21] ROUNDY, C. B., and K.D. KIRKHAM. Current technology of laser beam profile measurements. *Laser beam shaping*. Citeseer, 2014, pp. 463–524.

[22] KEAVENEY, J. Automated translating beam profiler for in situ laser beam spot-size and focal position measurements. *Review of Scientific Instruments*. 2018, Vol. 89, No. 3, pp. 035114. Available from DOI 10.1063/1.5022973.

[23] GUTTENOVA, J. Laser beam scanning by mechanical devices and CCD camera. In: *14th Slovak-Czech-Polish Optical Conference on Wave and Quantum As- pects of Contemporary Optics*. SPIE, 2006. pp. 342 – 349. Available from DOI 10.1117/12.638977.

[24] ALEXEEV, I., J. WU, M. KARG, Z. ZALEVSKY, and M. SCHMIDT. Determination of laser beam focus position based on secondary speckles pattern analysis. *Appl. Opt.* OSA, Sep, 2017, Vol. 56, No. 26, pp. 7413–7418. Available from DOI 10.1364/AO.56.007413.

[25] WASSERMAN, L. *Random Variables*. New York, NY: Springer New York, 2004. ISBN 978-0-387-21736-9.

[26] JOLLIFFE, I.T. *Principal component analysis*. 2nd ed ed. New York: Springer, 2002. ISBN 03-879-5442-2.

[27] PRICE, G. R. Extension of covariance selection mathematics. *Annals of Human Genetics*. 1972, Vol. 35, No. 4, pp. 485-490. Available from DOI 10.1111/j.1469-1809.1957.tb01874.x.

[28] *Scipy.optimize.least_squares*. [cit. 2022-04-06]. https://docs.scipy.org/doc/scipy/reference/index.html.

[29] MARTIN, J., G.D. MARTIN, and A.G. ASUERO. Intersecting Straight Lines: Titrimetric Applications. In: 2017. ISBN 978-953-51-3523-4. Available from DOI 10.5772/intechopen.68827.

[30] WERNER, T. *Optimalizace*. Praha, 2020.

[31] *InGaAs cameras*. [cit. 2022-02-13]. https://www.hamamatsu.com/eu/en/product/cameras/ingaas-cameras.html.

[32] *InGaAs area image sensor G13393-0909W* . [cit. 2022-02-13]. https://www.hamamatsu.com/content/dam/hamamatsu-photonics/sites/documents/99_SALES_LIBRARY/ssd/g13393-0909w_kmir1027e.pdf.

[33] *M Plan Apo NIR 20X , Item No. 378-824-5* . https://shop.mitutoyo.eu/.

[34] OPTICS, Edmund. *Optics and photonics catalog & resource guide — 2022* .

[35] GHOSH, S., D. FROEBRICH, and A. FREITAS. Robust autonomous detection of the defective pixels in detectors using a probabilistic technique. *Appl. Opt.* 2008, No. 47, pp. 6904-6924. Available from DOI https://doi.org/10.1364/AO.47.006904.

[36] ZHANG, J.X.J., and K. HOSHINO. *Molecular Sensors and Nanodevices: Chapter 5 - Optical Transducers*. Oxford: William Andrew Publishing, 2014. ISBN 978-1-4557-7631-3. Available from DOI https://doi.org/10.1016/B978-1-4557-7631-3.00005-3.

[37] JHGUCH. *Boxplot and a probability density function (pdf) of a Normal N(0,1σ²) Population.* [cit. 2022-05-13]. https://commons.wikimedia.org/wiki/File:Boxplot_vs_PDF.svg.